

# Microstructural Evolution of Dissimilar Metal Welds Involving Grade 91



SEAN ORZOLEK, JOHN DUPONT, and JOHN SIEFERT

Dissimilar metal weld failures between low alloy Cr-Mo ferritic steels and austenitic stainless steels made with Ni-base filler metals are typically observed along the fusion line. Such DMW failures often exhibit the onset of damage well before their expected service life. Failure is typically associated with a carbon-depleted region in the ferritic steel and formation of creep voids along a row of so-called Type I carbides. More recently, the formation of Type I carbides adjacent to a carbide-free ferrite band has also been observed in DMWs where the ferritic steel was a 9 pct Cr creep strength-enhanced ferritic steel. However, it has not been completely clarified whether these microstructural features formed during welding, post-weld heat treatment or service. In this study, single pass bead-on-plate welds were prepared on a Grade 91 steel substrate using commonly specified Ni-base weld metals; ENiCrCoMo-1, ENiCrMo-3, ENiCrFe-3, ENiCrFe-2 and EPRI P87 (ENiFeCr-4) and were characterized in the as-welded, post-weld heat treatment (PWHT) and aged conditions. The evolution of the ferrite band was found to form by a diffusion-controlled process and was observed after PWHT and aging associated with regions exhibiting steep concentration gradients in the partially mixed zone (PMZ). In this study, steep concentration gradients were observed along the toe of the weld whereas relatively shallow gradients were observed at the weld bottom-center, resulting in a discontinuous ferrite band along the fusion line during PWHT and aging. The variation in chemical gradients in the PMZ corresponded to different chemical potential gradients, which lead to differences in carbon diffusion during high-temperature PWHT and aging. The results of this study provide insight into potential solutions for minimizing the risk of failure in future applications.

<https://doi.org/10.1007/s11661-020-05715-2>

© The Minerals, Metals & Materials Society and ASM International 2020

## I. INTRODUCTION

DISSIMILAR metal welds (DMWs) in the power generation industry between Grade 91 (P91) and austenitic stainless steels are most commonly welded together using Ni-base filler materials.<sup>[1,2]</sup> These welds connect ferritic steels, used in the low-temperature regions of a power plant, to stainless steels, which are used in the higher temperature and more corrosive regions. A key characteristic of DMWs is the tendency for premature failure, which can lead to significant economic impact due to lost profits and repair costs.<sup>[3]</sup>

The general failure mechanism of DMWs involving low alloy, Cr-Mo ferritic steels (*e.g.*, Grade 22) has recently been reviewed in detail.<sup>[4]</sup> To summarize, the

sharp change in microstructure across the fusion line of DMWs in the as-welded condition forms due to a steep chemical concentration gradient across the partially mixed zone (PMZ), resulting in the formation of as-quenched martensite. Prolonged high temperature exposure during post-weld heat treatment (PWHT) or service results in carbon diffusion down the chemical potential of carbon (CPC) gradient from the ferritic base metal towards the austenitic fusion zone. In DMW failures involving Grade 22 steels, carbon diffusion leads to the formation of a row of carbides (Type I carbides) adjacent to a carbon-depleted soft zone on the ferritic side and a carbon-enriched hard zone on the austenitic side.<sup>[5]</sup> These large differences in microstructure and strength occur over very short distances across the fusion line (~ 50 to 100  $\mu\text{m}$ ). Concomitantly, locally high stresses can develop along the fusion line in the DMW from the differences thermal expansion coefficients (CTE) between the ferritic and austenitic steels. As a result of these factors, strain is concentrated in the weak, carbon-depleted zone near the fusion line, thus generating creep voids around the Type I carbides. Eventually the extent of damage is such that continued in-service

---

SEAN ORZOLEK and JOHN DUPONT are with the Lehigh University, 5 East Packer Ave, Bethlehem PA, 18015. Contact e-mail: smo216@lehigh.edu JOHN SIEFERT is with the Electric Power Research Institute, 1300 West WT Harris Boulevard Charlotte, NC 28262.

Manuscript submitted January 23, 2019.

Article published online March 12, 2020

growth leads to the formation of micro- and later macro-cracking. This observed mode of failure may be assisted by local contributors to an enhanced stress-state, temperature cycling or formation of a surface-connected oxide notch.

While Grade 22 DMW failures have been extensively studied, few studies have focused on failures involving Grade 91 DMWs. Work conducted to date on failures involving Grade 91 have demonstrated that failure also occurs along the fusion line where creep voids ultimately lead to failure.<sup>[6,7]</sup> Similar to DMWs involving lower Cr-Mo steels, failure is attributed to various microstructural features including the presence of a carbide-free ferrite band and Type I carbides along the fusion line. The carbides initially form in a spherical shape, but subsequently form a lenticular morphology with continued aging and alignment along the fusion line.<sup>[4,8–11]</sup> A recent study has observed these carbides in DMWs involving Grade 91.<sup>[12]</sup>

A recent study characterized service-induced damage in a DMW between Grade 91 and ENiCrFe-3 as shown in Figures 1(a) through (d).<sup>[13]</sup> This sample was subjected to a service temperature of 565 °C for approximately 125,000 hours prior to removal. Damage is postulated to have originated near the surface at the fusion line and propagated through the wall thickness along the fusion line due to the formation of creep voids along the interface between the carbide-free ferrite band and Type I carbides. This carbide-free ferrite band ranged in width from 1 to 3 μm and was only observed between the fusion line and the FCC/BCC interface (Figure 1(d)). A similar creep damage mechanism was recently observed in fusion welds involving IN740H, where creep failure was found to be associated with precipitation-free zones and coarsened precipitates.<sup>[14]</sup> Similar to the DMW service failure, creep voids were found to form between the precipitate-free zone and the coarsened secondary phase. In each case, strain

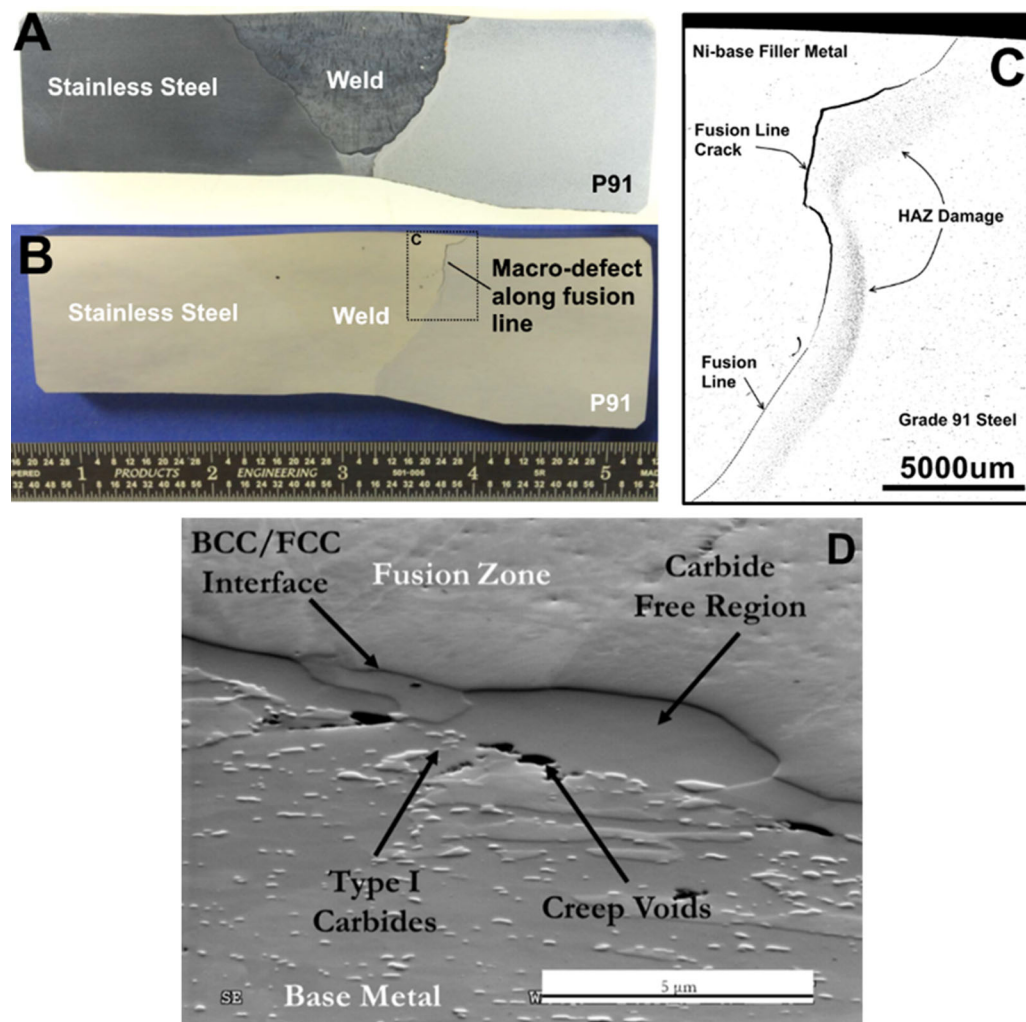


Fig. 1—DMW service failure after 125,000 h at 565 °C between P91 and ENiCrFe-3 with stereo-microscopy (a) etched, (b) as-polished, (c) light optical image highlighting the damage along the fusion line and heat affected zone (HAZ), and (d) scanning electron microscopy image of the damage tip along the fusion line.

localization within the precipitate-free zone appeared to be an important factor that contributed to failure.

Although the carbide-free ferrite band and Type I carbides were observed after service failure in the DMW described above, the condition of the microstructure near the fusion line in the as-welded, PWHT, and aged condition has not yet been reported in detail. Thus, it is currently not known whether these microstructural features form as a result of welding, PWHT, or service aging, and the formation mechanism has not yet been considered in detail for DMWs involving Grade 91. Therefore, the objective of this study is to understand how the microstructure evolves at the fusion line in the as-welded, PWHT and aged condition. This is conducted through microstructural analysis *via* electron microscopy as well as thermodynamic and kinetic modeling. The results of this study provide insight into potential solutions for minimizing the risk of failure in future applications.

## II. PROCEDURE

Single pass bead-on-plate DMWs were fabricated using P91 base metal and ENiCrCoMo-1, ENiCrMo-3, ENiCrFe-3, ENiCrFe-2 and EPRI P87 (ENiFeCr-4) electrodes using the shielded metal arc weld (SMAW) process. The welding process was performed manually using a consistent set of variables including a voltage of 25 V, amperage of 100 A and a travel speed of 8 in/min (203.2 mm/min). The measured compositions of the P91 base metal and filler wires used in this study are shown in Table I.

Samples were cross-sectioned from regions where the weld exhibited steady-state conditions and evaluated in the as-welded and 1-hour PWHT condition at 760 °C (1400 °F). Additional samples were subjected to a 1-hour PWHT at 760 °C and subsequently aged at 625 °C (1157°F) for 2000, 4000, 6000 and 8000 hours. Each sample was metallographically prepared to a final polish of 50 nm colloidal silica and etched with Vilella's etchant for the base metal and electrolytically etched with 10 pct oxalic at 2.5 V for 3 to 30 seconds for the fusion zone.

Light optical microscopy (LOM) was conducted on a Riechert-Jung® MeF3 metallograph. Scanning electron microscopy (SEM) was conducted on a Hitachi® 4300 FEG-SEM and a FEI® Scios Dual Beam microscope using an accelerating voltage of 15 kV and a beam current of 0.5 nA. Electron Backscatter Diffraction

(EBSD) was conducted using an EDAX Hikari Pro detector using an accelerating voltage of 15 kV and a beam current of 13 nA at a 70 deg tilt. Energy-Dispersive Spectroscopy (EDS) was conducted with an EDAX Octane Elite Detector under the same conditions as EBSD. The EDS and EBSD maps were collected simultaneously and exported using EDAX TEAM® software. Semi-quantitative EDS results were exported *via* ZAF correction using the EDAX TEAM® software. Nanoindentation was conducted using a Hysitron® PI-85 nanoindenter in an SEM with a berkovich diamond tip and a max load of 2500 μN and a trapezoidal load function.

Thermo-Calc/DICTRA® kinetic and thermodynamic models were used to simulate the carbon diffusion after PWHT and aging using the TCFE9 and TCNI8 databases for thermodynamic calculations and the MOB2 database for the kinetic calculations using a homogenization model.<sup>[15–17]</sup> A PMZ size of 50 μm was used for each simulation with 2.5 mm of base metal and 2.45 mm of weld metal for a total 5 mm length in the 2D diffusion simulation.<sup>[13]</sup> A bilinear chemical concentration gradient was used in the PMZ, which was in good agreement with the recent electron microprobe measurements for Grade 91 DMWs.<sup>[13]</sup>

Table II lists the compositions used for the Thermo-Calc/DICTRA® simulations for each alloy. The composition used for the fusion zone was calculated using an estimated dilution of 10 pct using the average value of every element with the exception of carbon for the filler metal and base metal, according to the AWS standard.<sup>[18,19]</sup> The maximum specification tolerance for carbon concentration was used for the base metal, and the minimum carbon concentration tolerance for each filler metal was used. This effectively produced the largest carbon concentration gradient, and therefore, presents the most intense condition for diffusion.

## III. RESULTS AND DISCUSSION

### A. Experimental

The location of the FCC/BCC interface was identified with EBSD analysis. Since EBSD cannot differentiate between ferrite (BCC) and martensite (body-centered tetragonal), the phase maps were used to identify the FCC/BCC interface. It is thus important to clarify the BCC nomenclature for martensite was used throughout this article in reference to the EBSD phase maps. Image

Table I. Chemical Compositions (Wt Pct) of Material Used

Alloy	C	Mn	Fe	P	S	Si	Cu	Ni	Co	Cr	Nb + Ta	Mo
P91	0.10	0.4	bal	0.013	0.0020	0.26	0.013	0.13	0.0112	8.58	0.061	0.94
ENiCrCoMo-1	0.12	1.8	1.1	0.010	0.0030	0.50	0.010	bal	11	24	0.6	9.0
ENiCrFe-2	0.030	2.9	7.8	< 0.0010	0.020	0.26	0.010	bal	0.048	14	1.52	0.8
EPRI P87 (ENiFeCr-4)	0.10	1.5	38	0.010	0.010	0.25	0.030	bal	—	9.4	—	1.9
ENiCrFe-3	0.054	6.4	8.1	0.0090	0.0060	0.44	0.020	bal	—	16	1.7	—
ENiCrMo-3	0.033	0.72	0.90	0.0040	0.0070	0.47	0.010	bal	—	21	3.4	9.1

quality (IQ) and inverse pole figure (IPF) maps were used to observe the grain and subgrain misorientation, where low angle subgrain boundaries were characterized to differentiate martensite from ferrite.<sup>[20,21]</sup>

### B. As-Welded Condition

The EBSD measurements were collected along the fusion line in the as-welded condition as shown in Figure 2(a) through (c) for the DMW between ENiCrCoMo-1 and P91. The phase map of this region is shown in Figure 2(a) with FCC in red and BCC in blue. The phase map overlaid on the IQ map in Figure 2(b) shows grain boundaries and sub grain boundaries as dark lines. The orientation of each of these grains and subgrains are shown by the IPF map in Figure 2(c). Large austenite grains are observed in the FCC region and several packets of martensite are observed in the BCC region. These are identified by the low angle

misorientations within the packet, which is in accordance with the low-angle subgrain boundaries of lath martensite.<sup>[20,21]</sup> These low angle misorientations are identified both in the IQ map as dark lines (subgrain boundaries) and in the IPF map as slight changes in orientation, which is consistent with a martensitic microstructure.<sup>[20]</sup> These observations were consistent for all DMWs evaluated, where a continuous band of martensite was observed adjacent to the FCC/BCC interface. Martensite formation along the fusion line after welding has been observed and explained in previous work.<sup>[6,22]</sup> The high-alloy content in the PMZ induces high hardenability that, when combined with the high cooling rates from welding, lead to martensite formation in the PMZ. As discussed below, formation of the ferrite band (as observed on damaged samples removed from service) is diffusion-controlled and thus cannot form with the short processing times associated with welding.

**Table II. Chemical Compositions (Wt Pct) used for Modeling**

Elements	P91	ENiCrFe-2	ENiCrFe-3	ENiCrMo-3	ENiCrCoMo-1	EPRI P87 (ENiFeCr-4)
C	0.120	0.030	0.03	0.03	0.0574	0.111
Co	0.00	0.00	0.00	0.00	11.2	0.00
Cr	8.48	15.0	15.4	19.8	20.6	8.94
Fe	89.5	11.7	22.8	18.6	10.8	45.6
Mn	0.445	1.50	6.31	0.00	0.00	0.00
Mo	0.920	1.44	0.268	7.34	8.15	1.82
N	0.0480	0.00	0.00	0.00	0.00508	0.00775
Nb	0.0690	1.57	0.00	2.35	0.00730	0.973
Ni	0.215	68.8	55.1	51.8	49.2	42.5
V	0.210	0.00	0.00	0.00	0.0221	0.0221

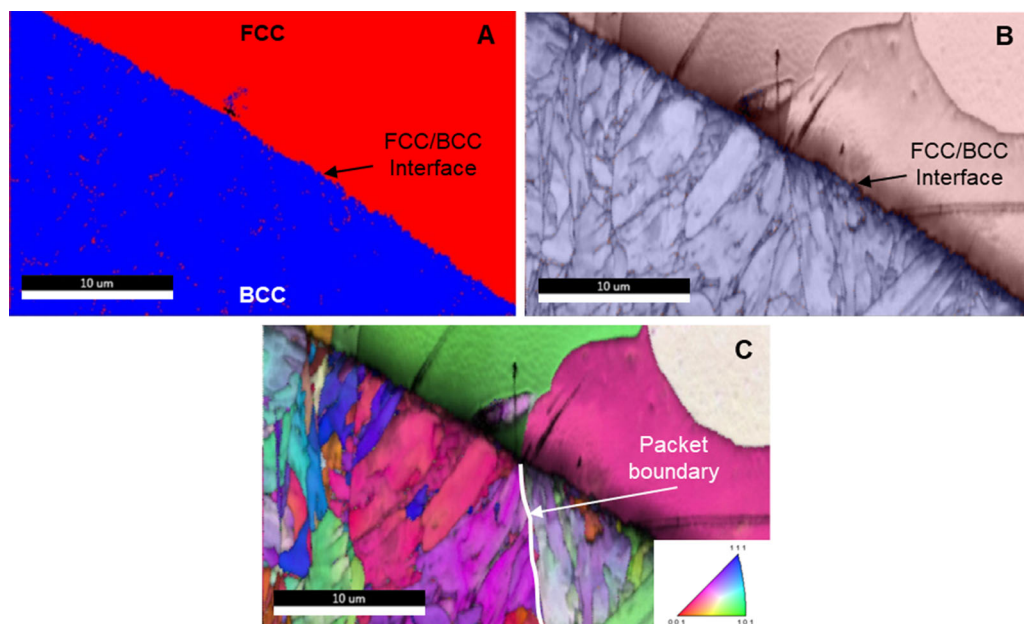


Fig. 2—EBSD of a DMW between P91- ENiCrCoMo-1 after welding with the (a) phase map (BCC is blue, FCC is red), (b) image quality (IQ) map overlaid with phase map and (c) inverse pole figure (IPF) map (Color figure online).

### C. PWHT Condition

After a 1-hour PWHT at 760 °C, an “interfacial band” (IB) was observed between the fusion line and the FCC/BCC interface for all DMWs. The IB is characterized by EBSD/EDS for the P91-ENiCrMo-3 DMW in Figure 3(a) through (f) and is representative of similar observations for the DMWs involving ENiCrFe-3, ENiCrFe-2 and EPRI P87 (ENiFeCr-4) after PWHT. The EBSD phase map overlaid on the SEM image (Figure 3(a)) demonstrates the IB to be BCC with no Type I carbides between the band and the base metal. The lath substructure from the P91 base metal extends into the IB (Figures 3(b) and (c)), terminating at the FCC/BCC interface. The subgrain boundaries suggest the microstructure of the IB is martensitic and is associated with the high hardenability of Grade 91 and the PMZ.<sup>[23]</sup> EDS maps for Cr, Mo, and Ni overlaid with the phase map of the same area are shown in Figures 3(d) through (f). These maps show that the IB is enriched in Ni and Cr when compared to the base metal. Identical analyses were conducted for the other DMW samples and the observations for the as-welded, PWHT and aged conditions are summarized in Table III.

For these DMWs, the IB likely transformed to austenite during PWHT but, due to the high hardenability, resulted in a martensitic transformation upon cooling. To assess this possibility, the composition of the martensite band was extracted from the EDS maps and is presented in Table IV. This composition was used with Andrew’s empirical calculations to estimate the

$Ac_1$ ,  $Ac_3$ , and  $M_s$  temperatures.<sup>[24]</sup> Although these equations were designed for compositions with less than 5 wt pct Ni and Cr, the calculations provide an estimation of these temperatures. Since the  $Ac_1$ ,  $Ac_3$ , and  $M_s$  temperatures are highly dependent on the carbon content and carbon cannot be accurately determined from EDS analysis, the carbon content was varied from 0 to 0.12 wt pct. This resulted in an estimated  $Ac_1$  temperature range of 719 °C to 723 °C and  $Ac_3$  temperatures in the range of 784 °C to 790 °C. This suggests that the IB was able to partially transform to austenite during PWHT at 760 °C, but the high hardenability of the PMZ P91 resulted in formation of martensite instead of ferrite on-cooling.<sup>[23]</sup> This is reinforced by the low, critical cooling rate of Grade 91 of approximately 0.2 °C/s and the empirically calculated  $M_s$  temperature, in the range of 130 °C to 139 °C.<sup>[24,25]</sup> This aspect has been observed in other DMW systems involving ENiCrMo-3.<sup>[6,22]</sup>

Unlike the other DMWs, the IB for the P91-ENiCr-CoMo-1 sample exhibits a different microstructure as shown by the EBSD/EDS characterization in Figures 4(a) through (f). The IB is BCC with a row of Type I carbides between the IB and base metal. The lath substructure from the base metal does not continue into the IB, instead a unique grain orientation is observed within the IB with no subgrain misorientation (Figure 4(c)). These observations indicate that the IB is ferritic. EDS maps overlaid with the phase map of this region show that the band is not enriched in Ni, Cr, or

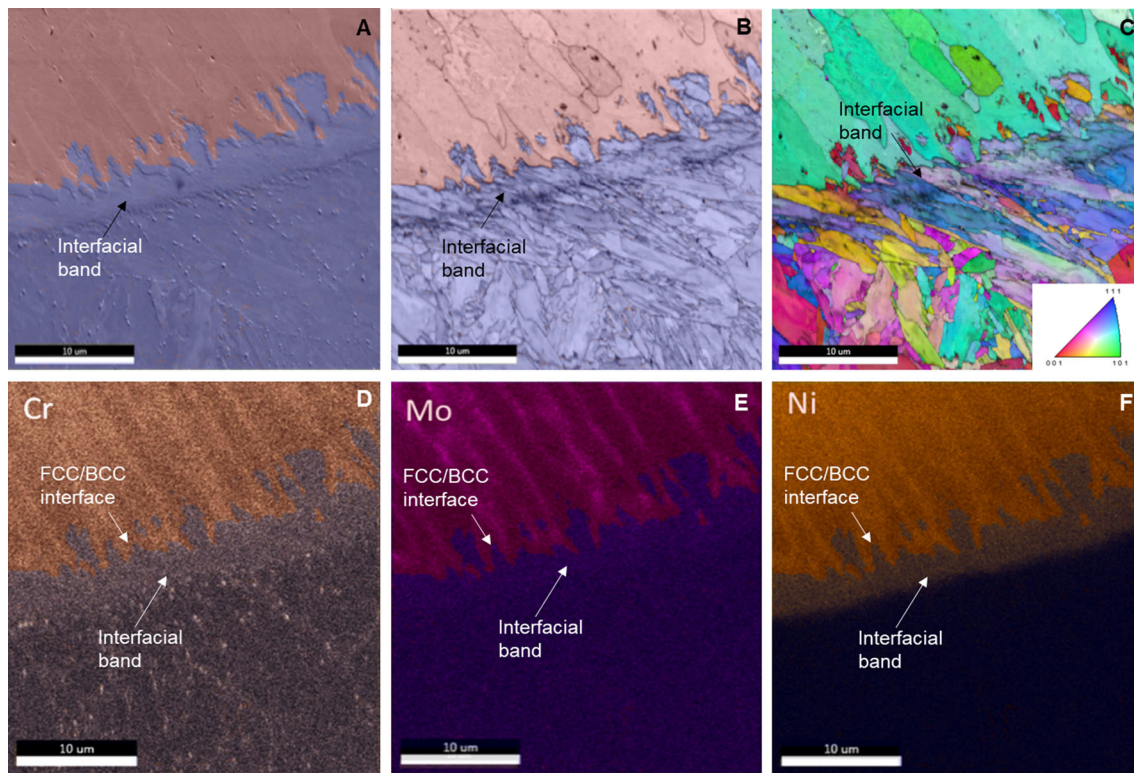


Fig. 3—EBSD/EDS overlaid with the phase map of the 1-h PWHT P91-ENiCrMo-3 DMW with (a) SEM image overlaid with phase map, (b) IQ overlaid with phase map, (c) IPF map, EDS maps overlaid with phase map for (d) Cr, (e) Mo, and (f) Ni.

**Table III. Summarized Microstructural Observations for each DMW**

Weld Metal	Microstructure After Welding	Microstructure After PWHT at 760 °C	625 °C Aging Time When Carbide-Free Ferrite Band and Type I Carbides were First Observed (h)
ENiCrFe-2	martensite	martensite	6000
ENiCrCoMo-1	martensite	ferrite	2000
ENiCrMo-3	martensite	martensite	4000
EPRI P87 (ENiFeCr-4)	martensite	martensite	6000
ENiCrFe-3	martensite	martensite	4000

**Table IV. Chemical Composition (Wt Pct) Comparison of Base Metal, Carbide-Free Ferrite Band, and Martensitic Band to Compositions Reported in Literature**

Technique	SEM EDS			WDS DuPont <i>et al.</i> Service Failure: Ferrite Band <sup>[13]</sup>	STEM EDS Clark <i>et al.</i> Ferrite Band <sup>[6]</sup>
	Base Metal	Ferrite Band	Martensite Band		
Nb	< 0.5 ± 0.1	< 0.5 ± 0.1	< 0.5 ± 0.1	—	< 0.5 ± 0.2
Mo	< 0.5 ± 0.1	0.8 ± 0.1	0.7 ± 0.2	< 0.5 ± 0.1	< 0.5 ± 0.3
V	< 0.5 ± 0.1	< 0.5 ± 0.1	0.7 ± 0.2	—	< 0.5 ± 0.1
Cr	9.9 ± 0.3	11 ± 0.4	11 ± 0.4	7.5 ± 0.3	8.1 ± 0.2
Mn	0.65 ± 0.1	0.7 ± 0.2	1.4 ± 0.2	0.6 ± 0.1	—
Fe	87 ± 5.4	85 ± 2.1	76 ± 1.7	89 ± 2.5	89 ± 0.5
Ni	1.5 ± 0.1	2.1 ± 0.3	10 ± 0.5	2.3 ± 0.2	1.8 ± 0.2

Mo and is carbide-free (Figures 4(d) through (f)). However, two distinct secondary phases are observed between the base metal and carbide-free ferrite band, with one exhibiting Cr enrichment and the other exhibiting Fe/Mo/Si enrichment. Similar observations were made for service aged DMWs involving P92 by Clark *et al.*, who characterized the microstructure through transmission electron microscopy as well as EDS. In their study, the Cr-rich Type I carbides were identified as the FCC  $M_{23}C_6$  carbides and the Mo-rich phase was identified as a hexagonal laves phase with a composition (all in weight percent) of 37Fe-11Cr-35-Mo-5Si.<sup>[6]</sup> Several studies have also reported the presence of laves phase along the fusion line for service aged P91 DMWs with enrichment of iron and molybdenum according to an  $(Fe)_2(Mo)$  stoichiometry.<sup>[26-29]</sup> The composition of the Mo-rich phase was extracted from the EDS map in Figure 4 resulting in a composition (on a weight percent basis) of 43Fe-13Cr-33Mo-4Si, suggesting that the phase observed is the  $(Fe,Cr)_2(Mo,Si)$  laves observed in Clark's work.<sup>[6]</sup>

The composition of the carbide-free ferrite band (Table IV) was used to empirically calculate the  $Ac_1$  and  $Ac_3$  temperatures, using the same method employed for the martensite band.<sup>[24]</sup> The calculated  $Ac_1$  temperature range is 853 °C to 856 °C and the calculated  $Ac_3$  temperature range is 897 °C to 903 °C, both of which are greater than the PWHT temperature used in this study of 760 °C. Therefore, the carbide-free ferrite band did not transform to austenite during PWHT and, since this region was adjacent to the FCC/BCC interface, likely became carbon depleted as has been observed in other DMW systems.<sup>[4]</sup>

#### D. Aged Condition

Each DMW system exhibited a carbide-free ferrite band and Type I carbides after aging up to 6000 hours as shown in Figures 5(a) through (e). Thus, none of the filler metals characterized in this study are immune to the formation of the carbide-free ferrite band and Type I carbides under the time and temperature conditions used here. However, there are differences in the time required to form these microstructural features (Table III).

The carbide-free band and associated Type I carbides became more pronounced for each DMW after 8000 hours of aging at 625 °C. The EBSD/EDS results of these microstructures are shown for the representative 8000-hour aged P91-ENiCrMo-3 DMW (Figures 6(a) through (f)). Similar to the ferrite band observed after PWHT for the P91-ENiCrCoMo-1 DMW, grains exhibiting no subgrain misorientation reside between the base metal and the FCC/BCC interface. The lack of subgrain misorientation is especially apparent in Figures 6(b) and (c) when comparing the misorientation of the ferrite band to that of the tempered martensite base metal. The EDS maps of this region overlaid with the phase map show that the ferrite is carbide-free and is adjacent to a row of Cr and Mo/Ni rich Type I carbides. These are likely to be Cr-rich  $M_{23}C_6$  Type I carbides and the Mo/Fe/Si rich Laves Phase which were observed for the P91-ENiCrCoMo-1 DMW after PWHT.

Although the carbide-free ferrite band was observed for all samples after aging for 6000 hours at 625 °C, this band was not continuous through the interface between the Ni-base weld metal and P91 substrate. An example of this is shown in Figures 7(a) through (f), which

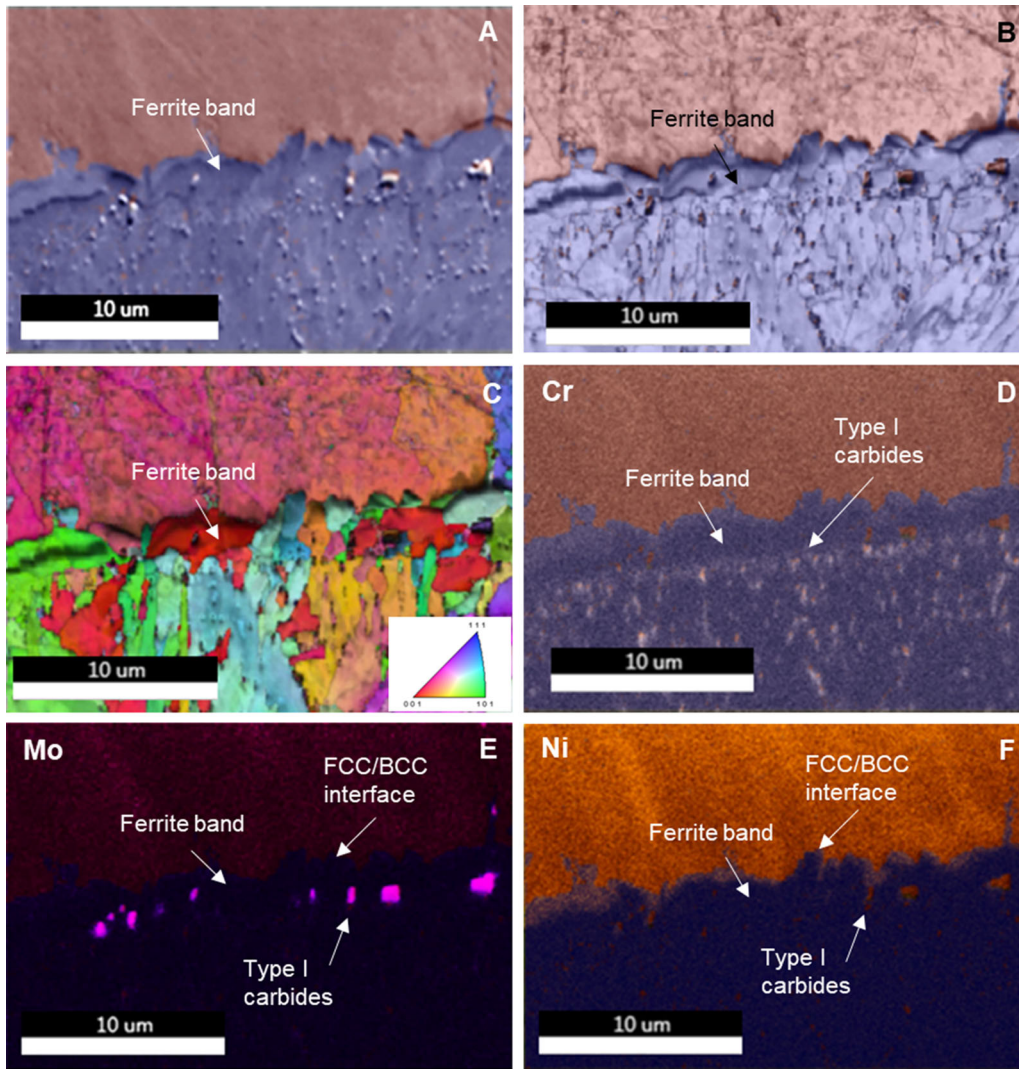


Fig. 4—EBSD/EDS overlaid with the phase map of the 1-h PWHT P91-ENiCrCoMo-1 DMW with (a) SEM image overlaid with phase map, (b) IQ overlaid with phase map, (c) IPF map, EDS maps overlaid with phase map for (d) Cr, (e) Mo, and (f) Ni.

displays the EBSD characterization of two different regions of a P91-ENiCrFe-3 DMW after aging 8000 hours at 625 °C. This sample exhibited a carbide-free ferrite microstructure along the toe of the weld (Figures 7(a) through (c)) and a martensitic structure towards the bottom-center of the weld (Figures 7(d) through (f)).

The average compositions of the carbide-free ferrite band, martensitic band and the base metal were extracted from EDS maps of the DMW's listed in the first two columns of Table V, which are averaged over the as-welded, PWHT and aged conditions as shown in Table IV. Although these compositions were averaged over different locations, different DMW's and different aging times, the standard deviation values of both the martensite and ferrite band are relatively low. This indicates that the ferrite and martensite bands have uniform composition of substitutional alloying elements regardless of the aging time or weld metal for which it was observed. These results are compared to two other compositional measurements from service failures which

exhibited a carbide-free ferrite band.<sup>[6,13]</sup> Although the compositions reported from the literature are for service failed samples exhibiting a ferrite band, the concentration of both Fe and Ni are similar to those measured in this study. The Cr content measured in the carbide-free ferrite band is higher for the samples in this study, likely due to differences in interaction volume of the electron beam in this study where a high beam current and a 70 deg tilt was used to simultaneously conduct EBSD/EDS characterization. This may have captured Cr characteristic X-rays from the Cr-rich Type I carbides adjacent to the band.

#### IV. KINETIC MODELING

Thermodynamic and kinetic modeling was conducted to simulate carbon diffusion during PWHT and aging. These simulations provide insight into the microstructural observations and assist in the comparison of the filler metals.

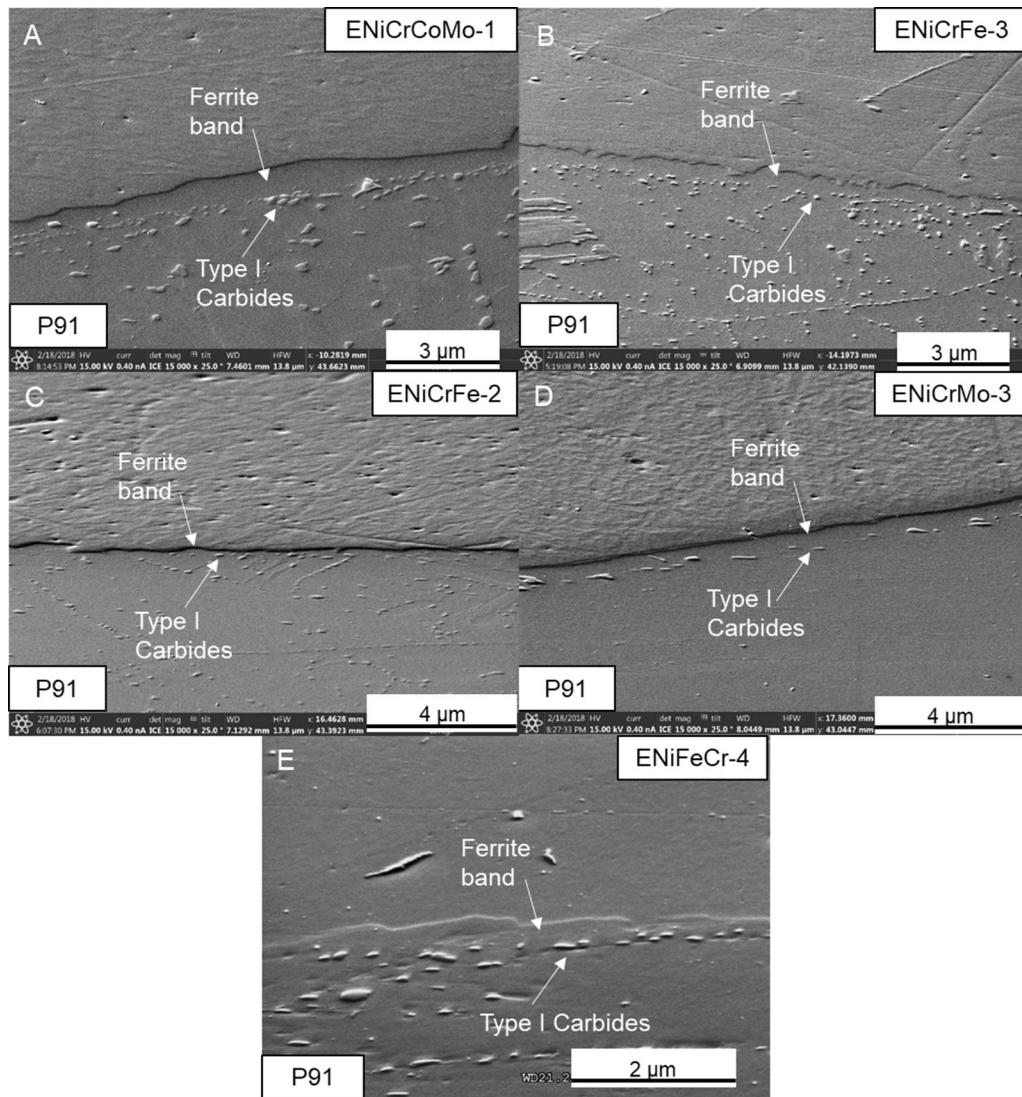


Fig. 5—SEM image after 6000 h of aging at 625 °C for DMWs between P91 and (a) ENiCrCoMo-1, (b) ENiCrFe-3, (c) ENiCrFe-2, (d) ENiCrMo-3, and (e) EPRI P87 (ENiFeCr-4).

### A. PWHT Condition

Figure 8 shows the CPC (8A), carbon concentration (8B) and phase fraction of minor phases (8C), plotted as a function of distance for the representative P91-ENiCrCoMo-1 DMW. The microstructural observations are in good agreement with the DICTRA® kinetic modeling at 760 °C where carbon depletion is predicted to occur in the BCC base metal (Figures 8(a) through (c)). The depletion of carbon in the base metal is due to a sharp discontinuity in the CPC at the fusion line, followed by a large, negative gradient in the PMZ. The system will act to relieve this sharp discontinuity and large gradient, which drives carbon to diffuse from the base metal to the FCC PMZ. This results in lower phase fractions of  $M_{23}C_6$  and  $M_6C$  carbides in the base metal when compared to the PMZ. Sigma and mu phases were predicted to form further into the FCC PMZ, which were not observed in this study and likely

require longer times to form. Identical simulations were conducted for DMWs involving alloys ENiCrFe-3, ENiCrMo-3 and ENiCrFe-2 which showed similar trends. However, the P91-EPRI P87 (ENiFeCr-4) DMW exhibits a different trend and is shown by Figures 9(a) through (c). For this DMW, there is a chemical potential gradient from the weld metal to the base metal, and the sharp gradient across the fusion line leads to a local carbon-enriched peak in the FCC PMZ.

Under the conditions of PWHT at 760 °C for 1-hour, there is not enough time for significant substitutional diffusion to occur as shown by Figure 10, where substitutional diffusion is negligible compared to interstitial diffusion.

Thus, reductions in the CPC gradient can only be achieved through carbon diffusion, where an increase in carbon concentration will lead to an increase in CPC and *vice versa*.<sup>[30]</sup> The change in carbon concentration over time ( $\delta C/\delta t$ ) is proportional to the second



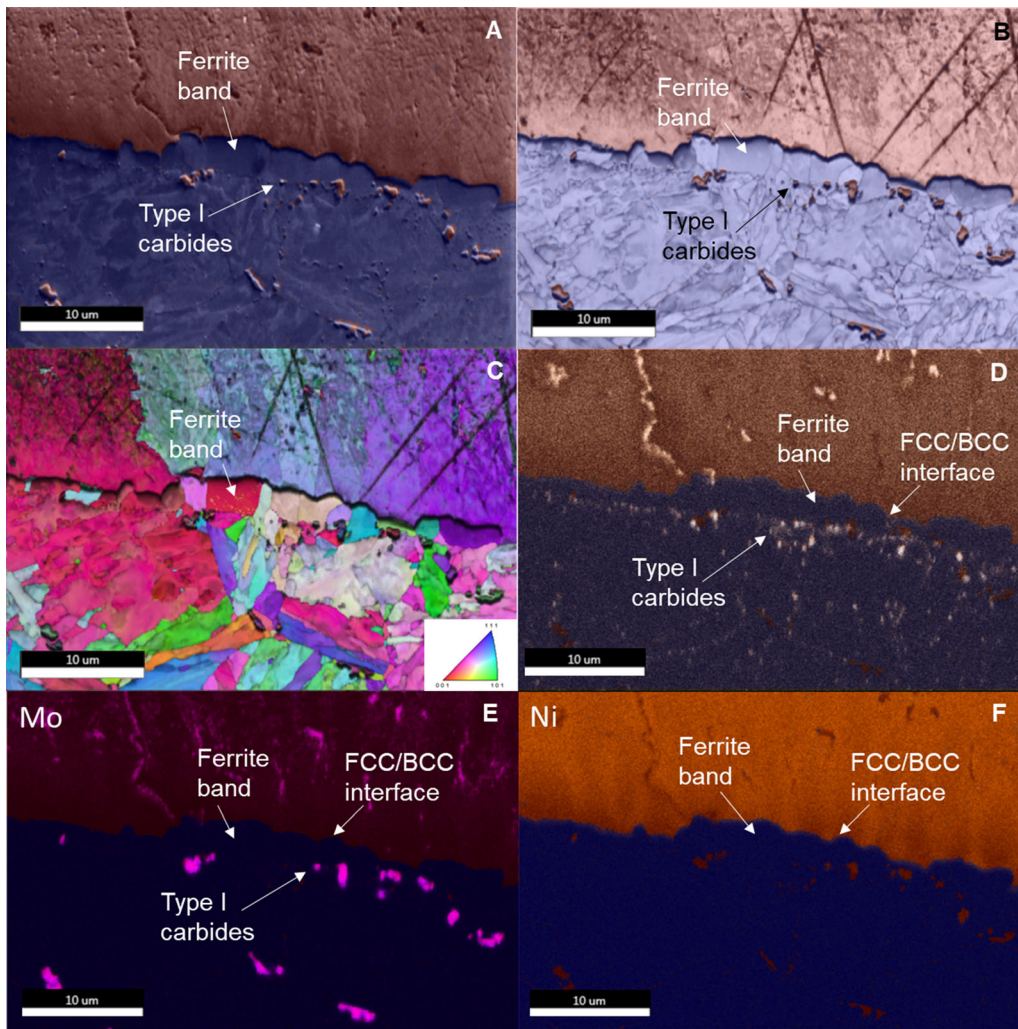


Fig. 6—EBSD/EDS overlaid with the phase map of the 8000-h aged P91-ENiCrMo-3 DMW with (a) SEM image overlaid with phase map, (b) IQ overlaid with phase map, (c) IPF map, EDS maps overlaid with phase map for (d) Cr, (e) Mo, and (f) Ni.

derivative of the CPC gradient ( $\delta\mu/\delta x$ ) according to Fick's second law (Eq. [1]).<sup>[31]</sup>

$$\frac{\delta C}{\delta t} \propto \frac{\delta^2 \mu}{\delta x^2} \quad [1]$$

Following Eq. [1], regions that exhibit a concave down CPC gradient (*i.e.*, near the fusion line) will result in the local reduction in carbon concentration over time. However, regions where the CPC gradient is concave up (*i.e.*, PMZ) will result in an increase in carbon concentration locally over time. Because of this, carbon can diffuse up the concentration gradient, resulting in further depletion of the base metal and enrichment of the FCC PMZ with increasing time (Figure 8(b)). However, within these relatively short time frames, complete equilibrium cannot be achieved. Hence, the overall CPC gradient can be reduced by a decrease in the CPC before the fusion line (*i.e.*, in the base metal) and an increase in CPC after the fusion line. Since substitutional diffusion is limited during a 1-hour PWHT, the change in CPC is proportional to the carbon

concentration. This effect is apparent by comparing the initial CPC curve to the curve after 3600 seconds of simulated exposure to 760 °C (Figure 8(a)). Lastly, carbon diffusion down the gradient near the FCC PMZ/weld metal region is not as pronounced as that observed at the fusion line. This can be attributed to the lower CPC gradient in that region and the lower diffusivity of carbon in FCC relative to BCC.

The local carbon depletion and enrichment near the fusion line depends largely on the magnitude of the initial CPC gradient at the fusion line. The magnitude of the gradient is, in turn, controlled by the width of the PMZ and the variation in composition as affected by dilution and filler metal composition. Although carbon will diffuse to reduce the chemical potential gradient, the initial difference in carbon concentration between the weld metal and the base metal does not have a significant effect on the CPC gradient (Figures 11(a) through (d)). Figures 11(a) and (b) provide results for a carbon concentration of 0.0574 wt pct for ENiCr-CoMo-1, and Figures 11(c) and (d) shows results where the carbon concentration is 0.12 wt pct for

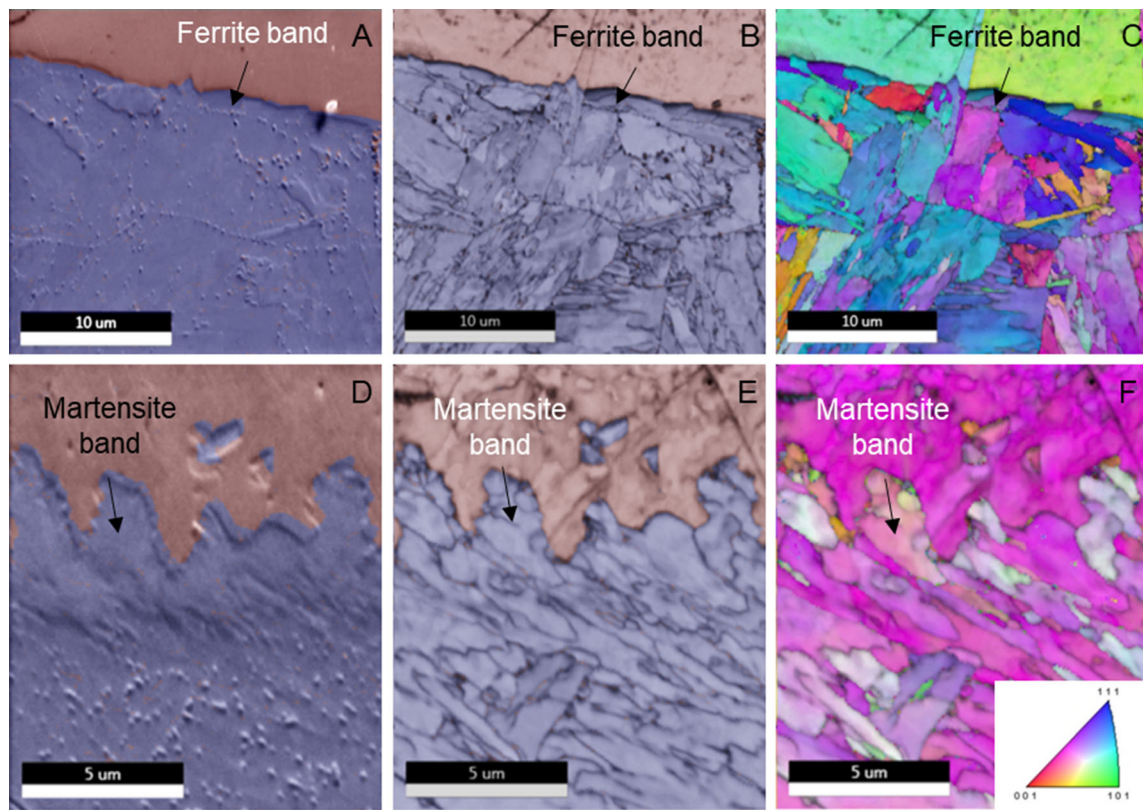


Fig. 7—EBSD for the (a to c) toe of the weld and (d to F) center of weld for a DMW between P91-ENiCrFe-3 after aging for 8000 h at 625 °C with, (a/d) SEM image overlaid with phase map (b/e) IQ map overlaid with phase map, and (c/f) IPF map.

Table V. Concentration Gradients Extracted from EDS Traces

Weld Metal	Sample	Microstructure	Concentration Gradient (Wt Pct/ $\mu\text{m}$ )	
			Fe	Ni
ENiCrCoMo-1	AW center of weld	martensite	- 2.7	1.8
	AW toe of weld	martensite	- 6.1	5.3
	1 h PHWT	ferrite	- 7.7	6.0
	2000 h aged center of weld	martensite	- 0.54	0.37
	2000 h aged toe of weld	ferrite	- 6.3	4.5
	8000 h aged	ferrite	- 6.7	5.4
	DICTRA®	—	- 9.2	5.7
ENiCrFe-3	8000 h aged toe of weld	ferrite	- 12	11
	8000 h aged center of weld	martensite	- 1.7	1.6
	DICTRA®	—	- 6.5	5.4
ENiCrMo-3	8000 h aged	ferrite	- 8.8	6.6
	1 h PWHT	martensite	- 1.6	1.4

ENiCrCoMo-1, matching the carbon concentration of P91. Even in the absence of an initial carbon concentration gradient, the CPC gradients are on a similar magnitude, indicating that these gradients are highly dependent on the substitutional alloying elements (Figures 11(a) through (c)). This leads to similar carbon concentration curves after PWHT where the base metal is depleted and the PMZ becomes enriched (Figures 11(b) through (d)).

Therefore, substitutional elements such as Ni, Cr and Mo have a much larger impact than carbon content on the CPC gradient. This is displayed in Figure 12 where the initial chemical potential gradient for each simulated DMW is plotted against the extent of carbon depletion and enrichment after a 1-hour PWHT. As expected, the DMWs with ENiCrCoMo-1 and ENiCrMo-3 filler metals, which exhibited the greatest CPC gradient at the fusion line, exhibit the most depletion in the base

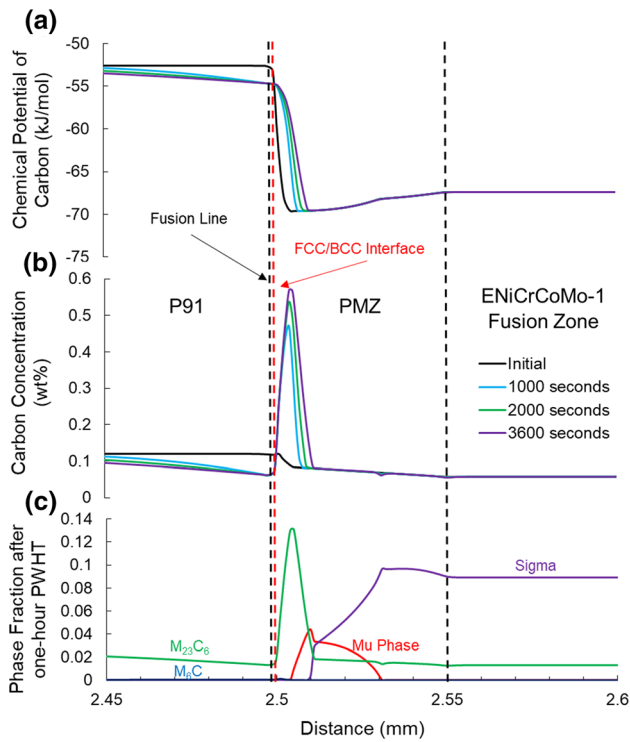


Fig. 8—DICTRA® simulation of the P91-ENiCrCoMo-1 DMW after a 1-h PWHT at 760 °C: (a) chemical potential of carbon, (b) carbon concentration, (c) phase fraction for minor phases after 1-h.

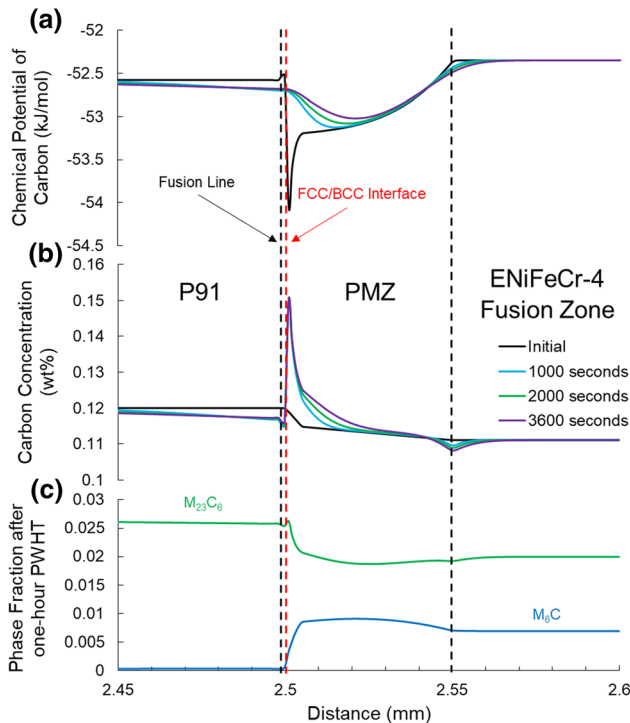


Fig. 9—DICTRA® simulation of the P91-ENiFeCr-4 DMW after a 1-h PWHT at 760 °C: (a) chemical potential of carbon, (b) carbon concentration, (c) phase fraction for minor phases after 1-h.

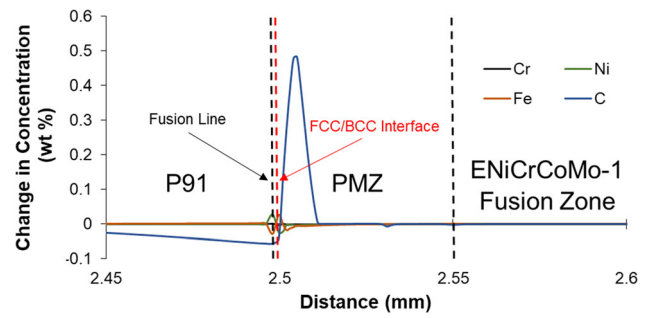


Fig. 10—DICTRA® comparison of the extent of interstitial and substitutional diffusion after a 1-h PWHT at 760 °C for the P91-ENiCrCoMo-1 DMW.

metal and enrichment in the PMZ. This is associated with high levels of carbide forming substitutional elements of Cr, Mo, and/or Nb in these alloys. Filler metals ENiCrFe-2 and ENiCrFe-3 show reduced carbon depletion, which can be attributed to reduced levels of Cr and Mo. The filler metal EPRI P87 (ENiFeCr-4) shows the smallest change in carbon concentration near the fusion line due to the purposeful, reduced Cr concentration in this filler metal.

## B. Aged Condition

DICTRA® simulations were conducted for the aged condition using the final compositions of the 1-hour PWHT simulations as the starting compositions for aging (Figures 13(a) through (c)). Because of this starting condition, there is an initial carbon concentration peak in the PMZ that is apparent after 3600 seconds (Figures 8(b) and 13(b)). This results in a peak in the CPC curve due to the carbon enrichment in the PMZ from PWHT (Figure 13(a)). This CPC peak is eliminated with aging time by the diffusion of carbon into the base metal and the PMZ. The CPC peak is observed in the aged simulation and not in the PWHT simulation due to the temperature dependence of the CPC as well as the location of the FCC/BCC interface in the PMZ. Carbon diffuses from the BCC base metal, down the CPC gradient into the FCC PMZ and, due to the lower diffusion rate of carbon in FCC compared to BCC, diffusion into the weld metal is inhibited and a carbon-enriched region forms. A carbon-enriched peak is observed along the fusion line, associated with an increase in phase fraction of  $M_{23}C_6$  and  $M_6C$  carbides, which agrees with the observation of Type I carbides. This is followed by a carbon- and carbide-depleted region between the fusion line and the FCC/BCC interface, which is where the BCC carbide-free ferrite band was observed. A carbon-enriched region was predicted to form in the FCC PMZ, which corresponds to  $M_{23}C_6$  carbides that are observed along austenite grain boundaries. With increasing aging time, carbon continues to diffuse from the base metal to the FCC PMZ resulting in further depletion of the region between

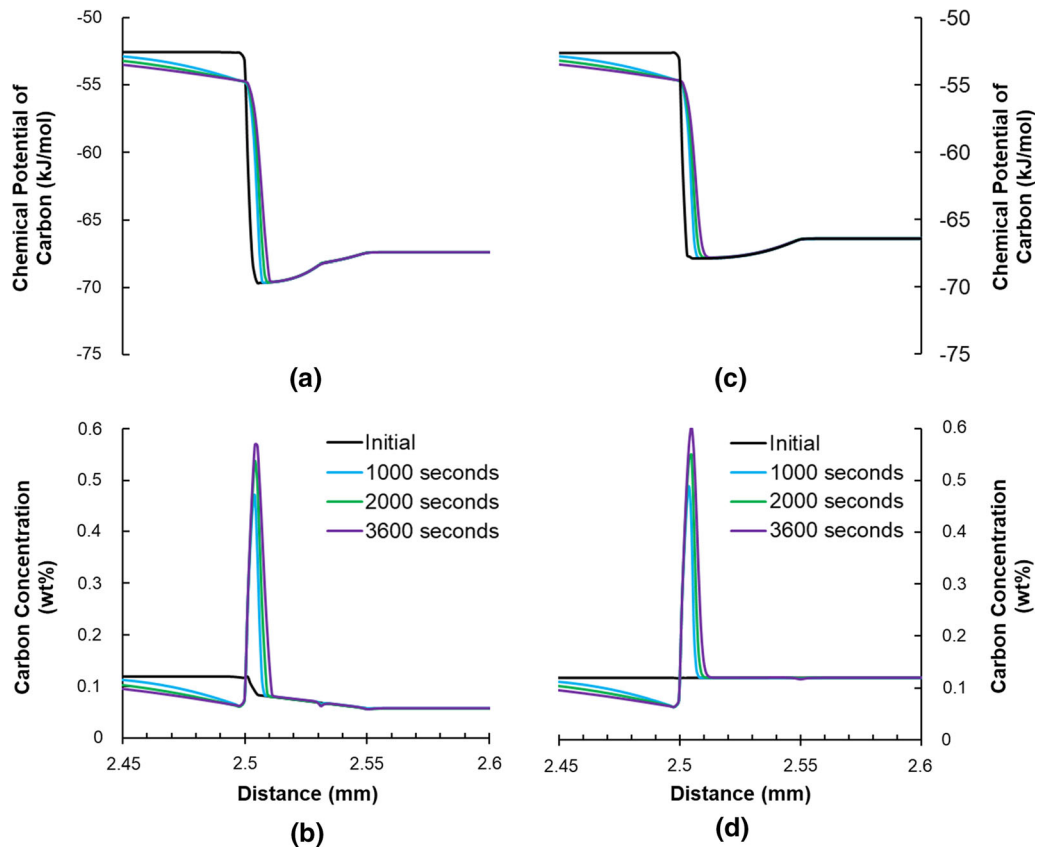


Fig. 11—Effect of nominal carbon concentration for the DICTRA® diffusion simulation of a P91/ ENiCrCoMo-1 DMW subjected to a 1-h PWHT at 760 °C with (a, b) the minimum allowed carbon concentration as shown in Table II and (c, d) the nominal carbon composition of the filler metal as shown in Table I.

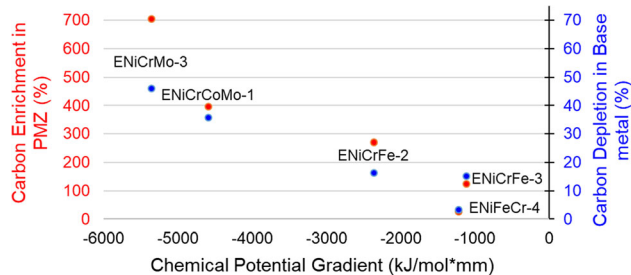


Fig. 12—Carbon enrichment and depletion of each DMW as a function of initial CPC gradient after a 1-h PWHT.

the FCC/BCC interface and fusion line. This observation serves to elucidate the reason for a more pronounced carbide-free ferrite band after 8000 hours of aging.

These observations were consistent for each DMW system, although the extent of carbon diffusion varied for each filler metal. However, the P91-EPR1 P87 (ENiFeCr-4) DMW (Figures 14(a) through (c)) shows that carbon diffuses from the weld metal into the base metal so that the FCC PMZ is carbon-depleted, and the base metal is enriched in carbon. Even though carbon diffuses from the FCC PMZ into the base metal, a carbon-depleted region forms between the FCC/BCC interface and fusion line, where the carbide-free ferrite

band was observed to form after service exposure (Figure 1).

A comparison plot of all DMW systems after a 1-hour PWHT at 760 °C and aging at 625 °C for 8000 hours is shown in Figures 15(a) and (b). Figure 15(a) provides a set of curves plotted as the difference in carbon concentration of each point (e.g., distance) after 1-hour PWHT and 8000 hours of aging from the initial compositions input into the simulation and Figure 15(b) exhibits the initial CPC curves plotted over the same distance. Although the extent of carbon enrichment and depletion varies for each DMW, corresponding to the differences in initial CPC gradients, a carbon-depleted region forms between the fusion line and FCC/BCC interface. This is in good agreement with the microstructural observations where the carbide-free ferrite band was observed for all DMWs after 8000 hours. However, there are differences in the time required to form these microstructural features (Table III). The differences in absolute time are associated with variation in the filler metal composition that controls the chemical potential gradient and concomitant carbon diffusion. The simulated change in carbon concentration after aging (Figure 15) is generally in agreement with the times where the ferrite band was observed. For example, DMWs with ENiCrCoMo-1 and ENiCrMo-3 are predicted to exhibit more carbon diffusion compared to DMWs involving ENiCrFe-2 and

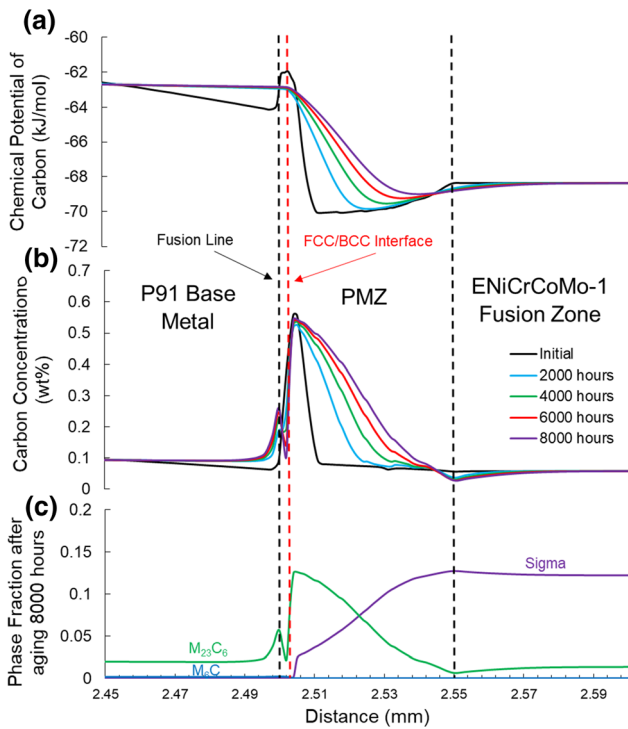


Fig. 13—DICTRA® simulation for the P91- ENiCrCoMo-1 DMW after a 1-h PHWT at 760 °C and aging for up to 8000 h at 625 °C: (a) chemical potential of carbon, (b) carbon concentration, (c) phase fraction for minor phases after aging 8000 h.

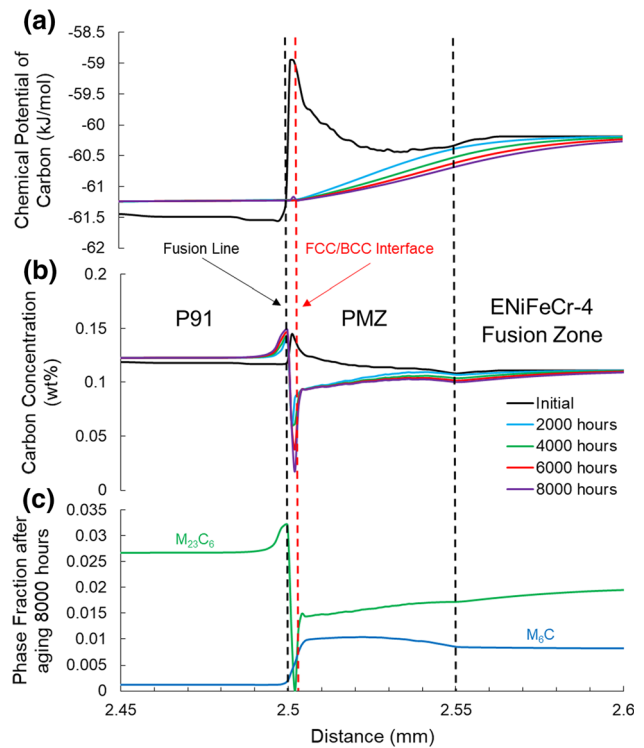


Fig. 14—DICTRA® simulation for the P91-ENiFeCr-4 DMW after a 1-h PHWT at 760 °C and aging for up to 8000 h at 625 °C: (a) chemical potential of carbon, (b) carbon concentration, (c) phase fraction for minor phases after aging 8000 h.

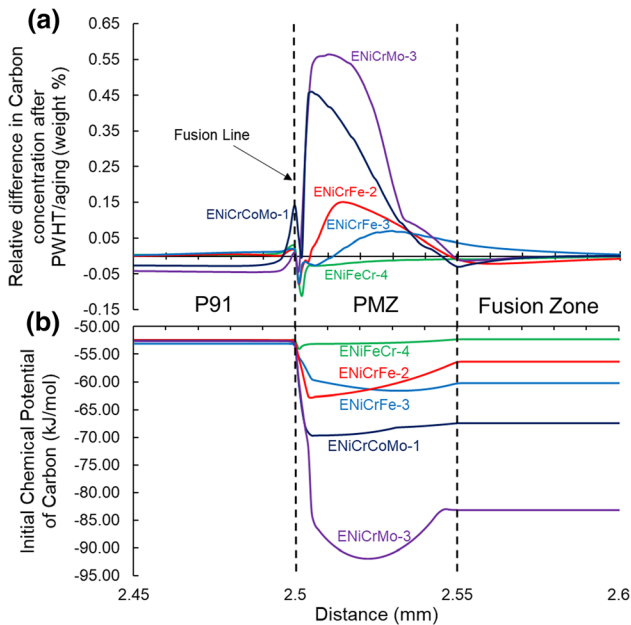


Fig. 15—DICTRA® simulation of each DMW displaying (a) difference in carbon concentration after a 1-h PWHT at 760 °C and aging at 625 °C for 8000 h and (b) initial chemical potential of carbon as a function of distance.

EPRI P87 (ENiFeCr-4) where the carbide-free ferrite band was observed after additional aging time.

### C. Gradient Comparison

Although the carbide-free ferrite band microstructure was observed after PWHT and aging, this band was not continuous along the fusion line as was shown for the 8000-hour aged P91-ENiCrFe-3 DMW (Figure 7). This sample exhibited a carbide-free ferrite microstructure along the toe of the weld (Figures 7(a) through (c)) and a martensitic microstructure (Figures 7(d) through (f)) towards the bottom-center of the weld.

The deviation in microstructure results from differences in chemical concentration gradients through the PMZ in the as-welded condition. An example of this is shown by EDS traces of the P91-ENiCrCoMo-1 DMW in the as-welded condition, which were taken along the toe of the weld (Figure 16(a)) and bottom-center of weld (Figure 16(b)) and are summarized in the schematic bead-on-plate weld (Figure 16(c)). These EDS traces are overlaid with the IQ and phase maps of the regions evaluated to identify the FCC/BCC interface and microstructure. The location of the EDS line trace is shown in green and the FCC/BCC interface is labeled by

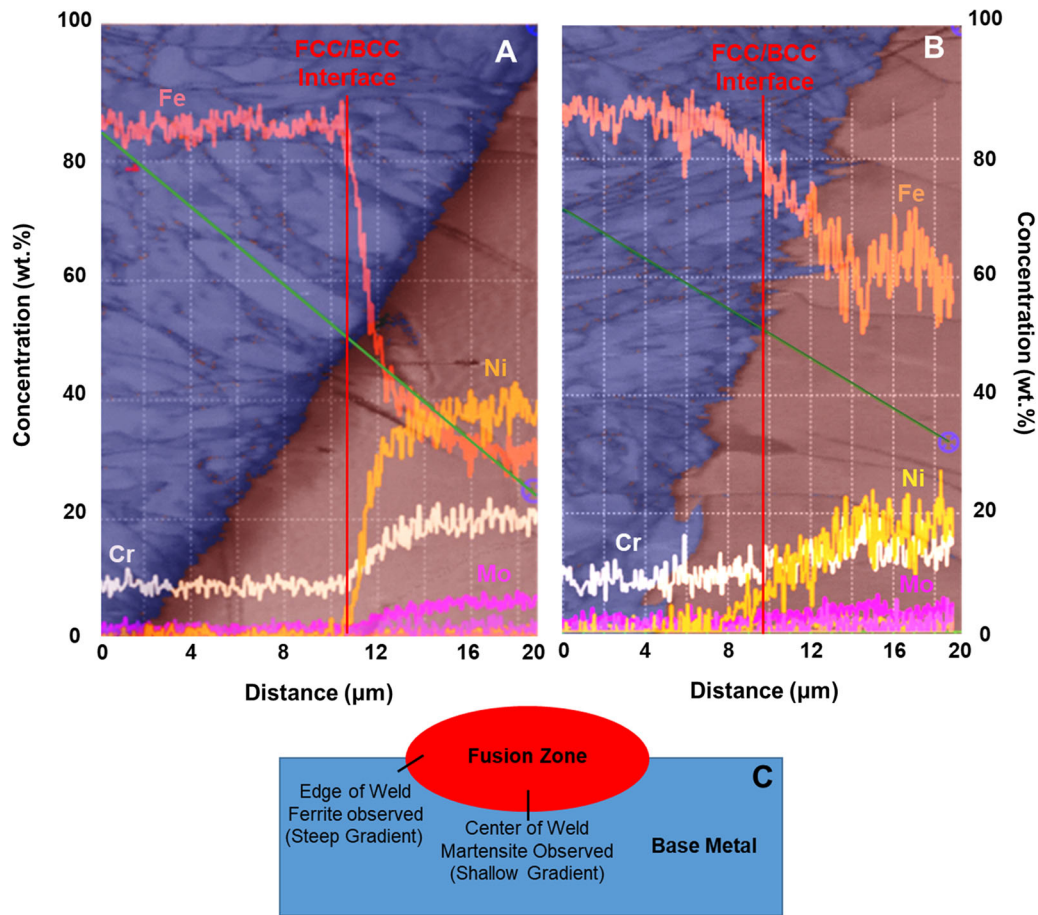


Fig. 16—EDS traces overlaid with IQ and phase maps for the as-welded P91-ENiCrCoMo-1 DMW (a) toe of weld, (b) bottom/center of weld with (c) schematic bead-on-plate weld summarizing the gradient and microstructural observations after PWHT and aging.

the red line. Although these traces were taken from the same sample, the observed concentration gradients varied, corresponding to differences in PMZ size, where the region near the toe of the weld (Figure 16(a)) has a  $\sim 7 \mu\text{m}$  PMZ and the region at the bottom-center of the weld has a PMZ size greater than  $20 \mu\text{m}$ . Similar trends were observed for other DMWs in this study, where steep concentration gradients (similar to Figure 16(a)) were observed near the toe of the welds, and the shallow concentration gradients (as shown in Figure 16(b)) were observed at the bottom-center of the welds (Figure 16(c)). This is summarized in Table V, where concentration gradients for Fe and Ni were extracted from EDS traces for regions within this study and are listed with the observed microstructures. The concentration gradients associated with the carbide-free ferrite band are an order of magnitude larger than the region where martensite was observed. This observation was not unique to this sample as the ferrite band was not continuous along the fusion line for any DMWs aged up to 8000 hours.

The variation of the chemical concentration gradients may be associated with differences in fluid flow velocities along the fusion line prior to solidification.<sup>[32]</sup> There are several driving forces for fluid flow during welding such as the buoyancy, Lorentz, surface tension and arc shear

stress forces.<sup>[32]</sup> Of these sources, the surface tension and arc shear stress drive fluid flow from the top-center of the weld towards the toe of the weld due to the differences in temperature, which lead to differences in fluid density and surface tension. However, as the bottom-center of the weld is not in close proximity to the surface of the weld, these forces will not impart as much mixing, thus leading to a reduced concentration gradient. This spatial difference in fluid flow velocity could be the cause of the difference in observed concentration gradients.

Therefore, the differences in observed microstructure after PWHT (Figures 3 and 4) are likely attributed to the differences in observed concentration gradients. The EDS traces overlaid with IQ and phase maps of the P91-ENiCrMo-3 and P91-ENiCrCoMo-1 DMWs are shown by Figures 17(a) and (b), respectively. Here, the P91-ENiCrCoMo-1 DMW (demonstrating the carbide-free ferrite band) exhibits a steep concentration gradient across the FCC/BCC interface (Figure 17(a)). In contrast, the P91-ENiCrMo-3 DMW (demonstrating the martensite band) exhibits a shallow concentration gradient across the FCC/BCC interface. Kinetic modeling of the PWHT condition (Figure 13) shows that the CPC gradient across the FCC/BCC interface is more severe than the gradient further into the PMZ.

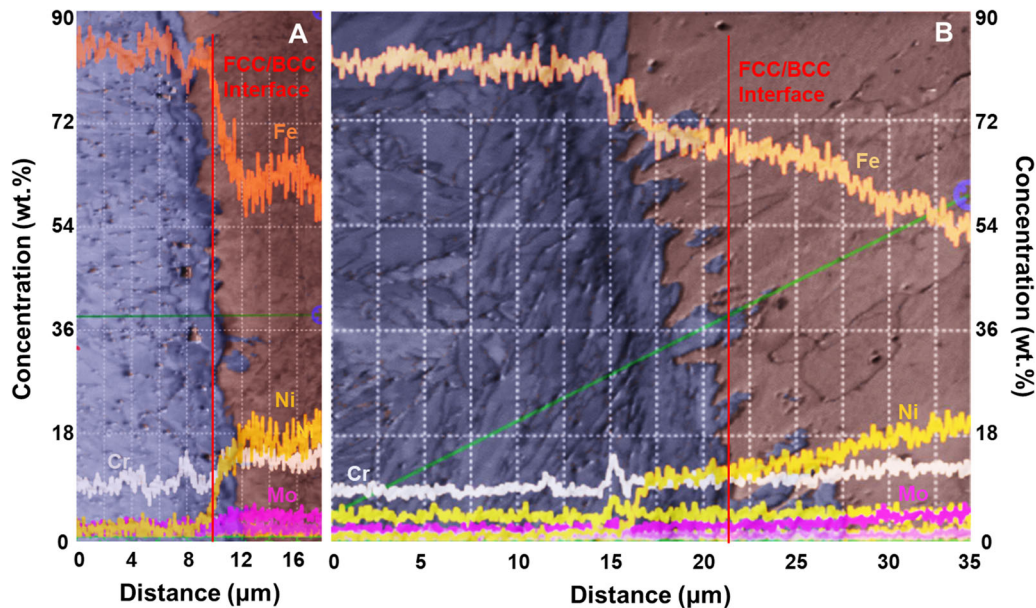


Fig. 17—EDS traces overlaid with phase maps for 1-h PWHT DMWs between (a) P91- ENiCrCoMo-1 as shown in Fig. 4 and (b) P91-ENiCrMo-3 as shown in Fig. 3.

Therefore, the differences in initial concentration gradients lead to differences in the extent of carbon diffusion after PWHT, explaining why ferrite was observed for the ENiCrCoMo-1 DMW and martensite was observed for ENiCrMo-3. Further evidence of this is supported by the 8000-hour aged P91-ENiCrFe-3 DMW which showed that the differences in microstructural observations are related to the gradient, independent of the filler metal used.

## V. MECHANICAL PROPERTY COMPARISON

To compare mechanical property differences of the carbide-free ferrite band, base metal and partially mixed zone, nanoindentation was used in place of micro-indentation due to the size limitation of the carbide-free ferrite band. Nanoindentation traces taken across the 8000-hour aged P91- ENiCrFe-3 DMW are compared to a P91- ENiCrFe-3 DMW service failure as shown in Figure 18.

In both the service failure and the 8000-hour aged DMW, no localized softened region is observed adjacent to the fusion line and the measured hardness is consistent between the two samples along the trace. This indicates that the room temperature hardness of the carbide-free ferrite band is not significantly different than the base metal or the PMZ and that the aged material is representative of the service failure. The similarity in room temperature hardness may be attributed to the small grain size of the ferrite band (1 to 3  $\mu\text{m}$ ) as well as the possibility that the region may be plastically deformed from the localized strain of the CTE mismatch along the fusion line. Although the ambient temperature hardness of the ferrite band is similar to that of the neighboring base metal and

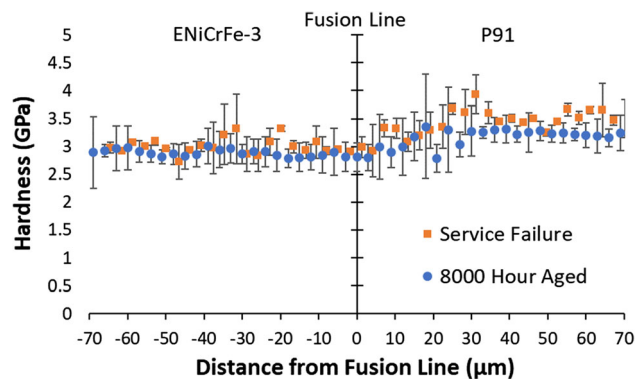


Fig. 18—Nanoindentation traces taken across the fusion line for the 8000-h aged P91- ENiCrFe-3 DMW compared to a P91- ENiCrFe-3 DMW service failure with data extracted from Ref. [13].

partially mixed zone, the small grain size and lack of carbides would render this region susceptible to the premature failure by accelerated creep deformation that is observed in the field samples.

## VI. RECOMMENDATIONS FOR MINIMIZING FAILURE

As discussed previously, the carbide-free ferrite band and the Type I carbides only evolve with exposure to high temperatures and times associated with PWHT and aging. Although the carbide-free ferrite band is not a direct result of welding (*i.e.*, the ferrite band does not form *during* welding), the difference in concentration gradients along the fusion line lead to differences in CPC gradient at elevated temperatures. Carbon diffuses from the base metal into the weld metal, down the CPC

gradient, resulting in a local carbon-depleted region prior to the FCC/BCC interface. This carbon diffusion can lead to localized carbide dissolution and degradation of the original martensitic lath morphology (Figure 19), resulting in a carbide-free ferrite microstructure. Due to the differences in the chemical concentration gradients, the carbide-free ferrite band and Type I carbides were commonly observed near the toe of the weld. As the toe of the weld will be exposed to the service environment, the formation of an oxide notch and the carbide-free ferrite band make this region the most susceptible to failure.<sup>[4,7,9,33,34]</sup> However, there are several possible practical solutions. For example, the concentration gradient along the fusion line could be reduced by increasing the dilution of the first weld pass. Alternatively, a filler metal with a composition intermediate to the base metal and filler metal could be used to make the first pass. A recent study has shown promise through the use of a graded transition joint involving Grade 22 and could also be applied to DMWs involving Grade 91.<sup>[35]</sup> Each approach would reduce the chemical potential gradient that is ultimately responsible for the ferrite formation. Of course, any investigation of these possible approaches would also require a thorough analysis of changes in local creep properties.

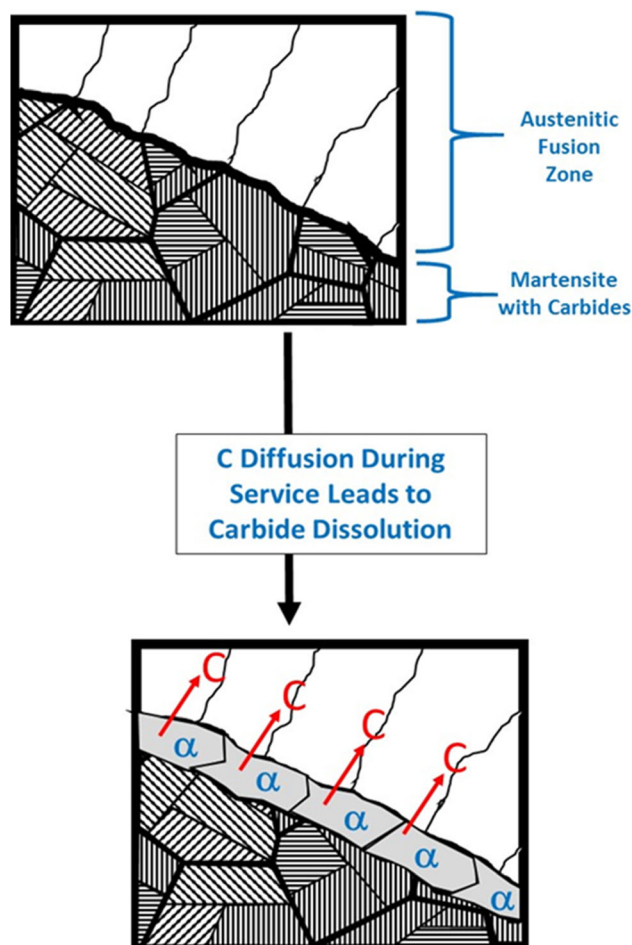


Fig. 19—Schematic mechanism for the carbide-free ferrite band formation during PWHT and aging.

## VII. CONCLUSIONS

Microstructural characterization was conducted on DMWs between P91 base metal and various Ni base filler metals to understand how the fusion line microstructure evolves during welding, PWHT, and long-term aging. The following conclusions can be drawn from this work.

1. The carbide-free ferrite band and Type I carbides do not form during welding, but form as a consequence of a diffusion-controlled process resulting from high-temperature exposure during PWHT and service-simulated aging.
2. For the aging conditions used in this work, the carbide-free ferrite band was observed for all filler metals after 6000 hours of aging at 625 °C and only formed in regions exhibiting steep chemical concentration gradients. The chemical concentration gradients were steeper along the toe of the weld when compared to the bottom-center. Therefore, carbide-free ferrite was more commonly observed along the toe of the weld and Ni-rich martensite was observed at the bottom-center of the weld after aging.
3. The carbide-free ferrite band results from carbon diffusing down the chemical potential gradient during high-temperature aging and PWHT in regions which exhibit a steep chemical concentration gradient after welding. This leads to local depletion of carbon in the martensite along the interface, thus producing a carbide-free ferrite band.
4. The carbide-free ferrite band and Type I carbides were observed for all DMW systems after 6000 hours of aging at 625 °C. However, some DMW systems exhibited the ferrite band earlier than others, which is related to the composition of the filler metal and the effect of the CPC. None of the filler metals included in this study are immune to the formation of this microstructure under the aging conditions utilized in this study.

## ACKNOWLEDGMENTS

The authors would like to express their appreciation to the Manufacturing and Materials Joining Innovation Center (Ma<sup>2</sup>JIC) and the National Science Foundation for providing funding for this study and the Electric Power Research Institute for their mentorship. The authors would also recognize Michelle Kent and Professor Rick Vinci for their assistance with the nanoindentation testing.

## REFERENCES

1. S.A. David, J.A. Siefert, J.N. Dupont, and J.P. Shingledecker: *Sci. Technol. Weld. Join.*, 2015, vol. 20, pp. 532–52.
2. S.A. David, J.A. Siefert, and Z. Feng: *Sci. Technol. Weld. Join.*, 2013, vol. 18, pp. 631–51.



3. B. Dooley and P.S. Chang: *Powerpl. Chem.*, 2000, vol. 4, pp. 197–203.
4. J.N. DuPont: *Int. Mater. Rev.*, 2012, vol. 57, pp. 208–34.
5. C. Sudha, V.T. Paul, A.L.E. Terrance, S. Saroja, and M. Vijayalakshmi: *Weld. J.*, 2006, vol. 85, pp. 71s–80s.
6. J. William, G. Clark, and G. Investigating: 2015.
7. J. Siefert and J. Parker: *Program on Technology Innovation: Guidelines and Specifications for High-Reliability Fossil Power Plants—Best Practice Guideline for Manufacturing and Construction of Grade 91 Steel to Austenitic Stainless Steel Dissimilar Metal Welds*, 2017.
8. J.D. Parker and G.C. Stratford: *Sci. Technol. Weld. Join.*, 1999, vol. 4, pp. 29–39.
9. J.D. Parker and G.C. Stratford: *Mater. Sci. Eng. A*, 2001, vol. 299, pp. 164–73.
10. J.D. Parker and G.C. Stratford: *J. Mater. Sci.*, 2000, vol. 35, pp. 4099–4107.
11. D.I. Roberts, R.H. Ryder, and R. Viswanathan: *J. Press. Vessel Technol.*, 1985, vol. 107, p. 247.
12. K. Laha, K.S. Chandravathi, P. Parameswaran, S. Goyal, and M.D. Mathew: *Metall. Mater. Trans. A*, 2012, vol. 43A, pp. 1174–86.
13. J.N. Dupont: *Microstructural Characterization and Modeling of Dissimilar Weld Failures Involving Grade 91*, vol. 18052, 2016.
14. D.H. Bechetti, J.N. DuPont, J.J. de Barbadillo, B.A. Baker, and M. Watanabe: *Metall. Mater. Trans. A*, 2015, vol. 46A, pp. 739–55.
15. J.O. Andersson, T. Helander, L. Höglund, P. Shi, and B. Sundman: *Calphad Comput. Coupling Phase Diagrams Thermochem.*, 2002, vol. 26, pp. 273–312.
16. H. Larsson: *Calphad Comput. Coupling Phase Diagrams Thermochem.*, 2014, vol. 47, pp. 1–8.
17. H. Larsson and L. Höglund: *Calphad Comput. Coupling Phase Diagrams Thermochem.*, 2009, vol. 33, pp. 495–501.
18. Special Metals: 2012, vol. 2012, pp. 1–12.
19. J.C. Lippold, S.D. Kiser, and J.N. DuPont: *Welding Metallurgy and Weldability of Nickel-Base Alloys*, Wiley, New York, 2011.
20. A.A. Gazder, F. Al-Harbi, H.T. Spanke, D.R.G. Mitchell, and E.V. Pereloma: *Ultramicroscopy*, 2014, vol. 147, pp. 114–32.
21. H. Kitahara, R. Ueji, N. Tsuji, and Y. Minamino: *Acta Mater.*, 2006, vol. 54, pp. 1279–88.
22. J.N. Dupont and C.S. Kusko: *Weld. J.*, 2007, vol. 86, p. 51.
23. M. Łomozik and A. Zielińska-Lipiec: *Arch. Metall. Mater.*, 2008, vol. 53, pp. 1025–34.
24. K.W. Andrews: *J. Iron Steel Inst.*, 1965, vol. 203, pp. 721–27.
25. Vallourec & Mannesmann Tubes: *The T/P91 Book*, 1999.
26. C.G. Panait, W. Bendick, A. Fuchsmann, A.F. Gourgues-Lorenzon, and J. Besson: *Int. J. Press. Vessel. Pip.*, 2010, vol. 87, pp. 326–35.
27. J. Hald: *Materials at High Temperatures*, Maney Publishing, London, 2004, vol. 21, pp. 41–46.
28. A. Di Gianfrancesco, S. Tiberi Vipraio, and D. Vendit: *Procedia Eng.*, 2013, vol. 55, pp. 27–35.
29. G. Dimmler, P. Weinert, E. Kozeschnik, and H. Cerjak: *Mater. Charact.*, 2003, vol. 51, pp. 341–52.
30. J.P. Galler, J.N. DuPont, S.S. Babu, and M. Subramanian: *Metall. Mater. Trans. A*, 2019, vol. 50A, pp. 2765–83.
31. D.A. Porter, K.E. Easterling, and M.Y. Sherif: *Phase Transformations in Metals and Alloys*, CRC Press, Boca Raton, 2009.
32. S. Kou: *Welding Metallurgy*, 2002.
33. J.E. and W.G. G. Campbell: *Trends Weld. Res. United States*, 1981, pp. 443–70.
34. R. Nicholson: *Met. Technol.*, 1984, vol. 11, pp. 115–24.
35. J.P. Galler, J.N. DuPont, S.S. Babu, and M. Subramanian: *Metall. Mater. Trans. A*, 2019, vol. 50, pp. 2201–17.

**Publisher's Note** Springer Nature remains neutral with regard to jurisdictional claims in published maps and institutional affiliations.